

Flux Tube Dynamics

Oskar Steiner

*Kiepenheuer-Institut für Sonnenphysik, Schöneckstrasse 6
D-79104 Freiburg, Germany, steiner@kis.uni-freiburg.de*

Abstract. We propose that the observed fragmentation of magnetic elements is due to their inherent liability to the interchange instability. The convective collapse and numerical simulations of the formation of intense magnetic flux sheets including spectral signatures of the formation process are discussed. We suggest that the mean downflow measured in magnetic elements is due to a fraction of an ensemble of magnetic elements being in the formation phase at any given time. It is shown that observed Stokes V profiles of magnetic elements are actually an average of spatially strongly varying profiles with a delicate balance of positive and negative contributions to the area asymmetry.

1. Interchange Instability of Small Magnetic Flux Tubes

Magnetic elements, when observed at disk center, are usually best visible in “G-band filtergrams”, which are typically obtained with a wide-band filter of 1.2 nm FWHM bandpass centered around 430.5 nm. In this wavelength region, the solar spectrum shows vibration-rotation bands of the CH-molecule, which probably act to enhance the contrast of magnetic elements. First observations of the network in this wavelength window, named G-band by Fraunhofer, have been carried out by Muller (1985) at the Pic du Midi observatory in the French Pyrénées. More recently, this observational technique has been applied at the Swedish vacuum tower telescope on La Palma, where time series of up to 4 h under excellent seeing conditions have been obtained (Berger *et al.*, 1995, 1998; Berger and Title, 1996). The myriad of bright grains or “crinkles” that are visible in these images are known as *G-band bright points* and they can be taken as good proxies for magnetic elements according to Berger (1996).

Time series of G-band filtergrams (Berger and Title, 1996) reveal a strongly dynamic evolution of magnetic elements. They are located in intergranular lanes and at vertices of granules and move along intergranular lanes with velocities up to 5 km s^{-1} . Frequently, bright points split into smaller ones, while the formation of larger points by coalescence of two or more fine points is also observed. The lifetime of a single bright point, *i.e.*, the time period from its first appearance as an isolated object to its fragmentation, coalescence with other bright points, disappearance (possibly due to cancellation with opposite polarity elements), or fading, is of the order of the granular life time of 6–8 min.

One ubiquitous process that seems to act over the whole range of point sizes is the *fragmentation of bright points*. Correspondingly, the number of points

increases with decreasing diameter down to the resolution limit of the G-band images of about 0.3 arcsec. It is observed that the fragmentation of bright points is often the result of a perturbation by surrounding granules, leading to a deformation of the bright point prior to its breakup. In the following we explain this observation in terms of the fragmentation of magnetic elements due to their liability to the interchange instability, an inherent property of flux tubes, first noticed by Parker (1975) and Piddington (1975).

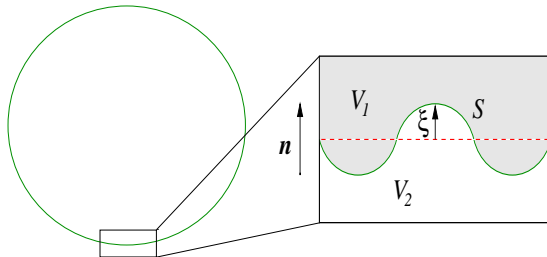


Figure 1. Cross section of a cylindrical flux tube (left) and an enlarged portion of the surface with interchange of magnetic with non-magnetic plasma (“fluting”) taking place.

If the surface of a cylindrical straight flux tube (Fig. 1) is perturbed in such a way that the volumes occupied by the magnetic and non-magnetic plasma remain the same, then the total energy of the configuration does not change, meaning that no effort is needed to deform the flux-tube surface. In a gravitationally stratified medium, the situation is somewhat more complicated. In summary it can be said that vertically oriented axisymmetric flux tubes in a stratified atmosphere are stable against interchange instability only if they expand strongly enough with height, so that buoyancy can act to stabilize the tube (Meyer *et al.*, 1977). This is the case for sunspots or pores but *not* for tubes with a magnetic flux smaller than about 10^{20} Mx, a limit well above the typical flux of magnetic elements of 5×10^{17} Mx.

The instability can be remedied if the magnetic field is twisted, in which case the toroidal field component acts like a “surface tension” inhibiting the interchange from occurring, or if the flux tube is surrounded by a whirl flow in the height range where the interchange instability occurs, as was first noticed by Schüssler (1984). If we assume this whirl flow with density ρ_e to possess a sole tangential (toroidal) component v_ϕ and the plasma within the tube to be at rest, the corresponding criterion for stability is

$$\frac{1}{4\pi} B_z \left. \frac{dB_r}{dz} \right|_S - \rho_e \frac{v_\phi^2}{R} < 0, \quad (1)$$

where R is the flux-tube radius and the index S indicates that the derivative has to be evaluated along the flux-tube surface. Note that a growing radial magnetic field strength with height destabilizes, whereas an azimuthal velocity has a stabilizing effect. Contrary to intuition, a flow along the tube surface in vertical direction ($v_z \neq 0$, not included in Eq. 1) would have a destabilizing effect.

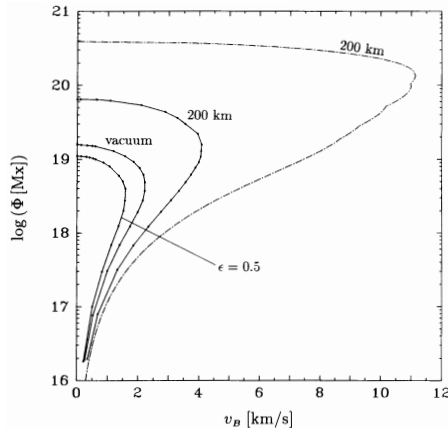


Figure 2. Minimal toroidal velocity component ($v_\phi = v_B$) on the flux-tube surface required for stability against fluting as a function of total magnetic flux and for various atmospheric combinations. “vacuum” refers to flux tubes that are completely evacuated. The outermost (dash-dotted) curve results when adopting the thin flux-tube approximation.

Bünthe et al. (1993b) found the necessary velocity for stabilizing small-scale flux tubes to be $2\text{--}4 \text{ km s}^{-1}$ on the tube surface, depending on the flux-tube diameter, the field strength, and the adopted atmosphere within and outside the flux tube (Fig. 2). It is likely that a bathtub effect develops at vertices of granules leading to the desirable whirl flow, but it will probably be disturbed on the granular time scale of about 6 min. Observation of this whirl flow is difficult since spectroscopy on a scale of $0.1''$ or local correlation tracking on subarcsecond scales (Simon & Weiss, 1997) is required.

Bünthe (1993) shows that in many cases the interchange instability of flux tubes is only severe in a limited height range around $\tau_c = 1$ so that single magnetic elements resulting from fragmentation at the solar surface are again bundled up into a larger, stable flux tube sufficiently far below and above the surface.

2. Formation of Photospheric Magnetic Flux Tubes

In the preceding section we have shown that magnetic flux tubes are subject to continuous fragmentation, presumably due to their inherent liability to the interchange instability – yet we know that over 90% of the magnetic flux in quiet Sun regions is concentrated into intense magnetic flux tubes with a field strength of $1\text{--}2 \text{ kG}$. Consequently, there must be an efficient process that reassembles weak field flux-tubes and/or continuous weak magnetic field into intense magnetic flux tubes. It is well known that due to the “frozen-in condition” of the magnetic field in the photospheric solar plasma, the field is swept to and along the boundaries of supergranular cells and to the intergranular lanes by the local horizontal flow (e.g., Parker, 1963; Weiss, 1966; Galloway *et al.*, 1977).

Subsequently, the magnetic field is further intensified by the *superadiabatic process* (Parker, 1978), which operates as follows. Assuming the downflowing gas inside the nascent magnetic flux tube to behave like a thermal insulator (because the magnetic field suppresses convective heat transfer) its temperature increases nearly adiabatically with depth. The important point is that the upper 3 Mm of the convection zone is significantly superadiabatic. This situation leads to a growing temperature deficit of the descending gas within the tube with respect to the surroundings, which implies a strong compression of the gas including the frozen-in magnetic field. At and above the surface ($\tau_{500} = 1$), the horizontal inflow of plasma into the forming tube is suppressed by the growing field and the downflow is neither replenished from the top because of the vanishingly small density there (Schüssler, 1990). Thus, the flux tube becomes almost evacuated throughout the photosphere and the field strength is limited only by the gas pressure of the surrounding atmosphere leading to a strength of up to 1800 G at the continuum optical depth unity of the surrounding atmosphere.

While the superadiabatic effect as described by Parker (1978) captures an essential point of the flux intensification process, deeper insights can be gained by considering the system of MHD-equations that govern this process. Based on a linear analysis of the vertical motion in a slender flux tube by Roberts and Webb (1978), Spruit and Zweibel (1979) derived a critical value $\beta_{\text{crit}} = p_g / (B_{\text{crit}}^2 / 8\pi) \approx 1.8$, above which limit convective instability ensues, which leads to a downflow and thus to field intensification by the superadiabatic process. Webb and Roberts (1978) as well as Unno and Ando (1979) came to a similar conclusion. Spruit (1979), using a quasi static approach, computed the final state to which this instability, which he called *convective collapse*, leads to. Nonlinear numerical solutions of the same problem have been obtained by Venkatakrisnan (1983) and Hasan (1984). Hasan (1985) and Venkatakrisnan (1985) have taken non-adiabatic effects into account, which arise from radiative heat exchange between the atmosphere and the embedded flux tube. A linear stability analysis including non-adiabatic effects was carried out by Webb and Roberts (1980), Venkatakrisnan (1986), and Hasan (1986). Further progress in treating radiative exchange was achieved by Massaglia *et al.* (1989), while Takeuchi (1993, 1995) stresses the importance of the adopted boundary conditions. Unlike to previous calculations with closed bottom boundary conditions he finds a static final state for the intense flux tube rather than an overstable solution. Takeuchi (1999) shows that for sufficiently large initial radii and plasma β the instability may become strong enough to induce an upward traveling *rebound shock* that reverses the magnetic flux intensification.

All these calculations rely on the thin-flux-tube approximation, make use of an initial state with constant plasma β along the flux-tube axis, and neglect the perturbation of the surrounding plasma by the flux tube as well as any interaction between the surrounding convective flow and the flux tube.

In order to overcome these limitations, while at the same time keeping the number of free parameters as small as possible, one has to solve the system of the magnetohydrodynamic (MHD) equations in a computational domain that includes the atmospheric layers most critical to the driving of the convective collapse instability and that is wide enough to encompass a sufficiently large environment of the flux tube. Thus, at least two spatial dimensions – depth

and one horizontal direction – are required. Since radiative cooling plays a decisive role in the intensification process and since one wishes to include the photospheric part in a manner as realistically as possible (*e.g.*, for the subsequent derivation of synthetic spectral lines), the inclusion of radiation transfer is an indispensable requirement.

A simulation of the magnetic field intensification that fulfills these requirements was carried out by Grossmann-Doerth *et al.* (1998), where they solved the following system of equations:

$$\frac{\partial \rho}{\partial t} = -\nabla(\rho \mathbf{v}), \quad (2)$$

$$\rho \frac{\partial \mathbf{v}}{\partial t} = -\nabla p - \frac{1}{4\pi} \mathbf{B} \times (\nabla \times \mathbf{B}) + \rho g_{\odot} \mathbf{z}, \quad (3)$$

$$\frac{\partial \mathbf{B}}{\partial t} = \nabla \times (\mathbf{v} \times \mathbf{B}), \quad (4)$$

$$\frac{\partial e}{\partial t} = -\nabla \left[\mathbf{v} \left(e + p + \frac{B^2}{8\pi} \right) - \frac{1}{4\pi} (\mathbf{B} \cdot \mathbf{v}) \mathbf{B} + q \right], \quad (5)$$

$$\nabla \mathbf{B} = 0, \quad (6)$$

$$e = \rho \epsilon + \frac{1}{2} \rho v^2 + \frac{B^2}{8\pi} + \rho g_{\odot} z. \quad (7)$$

Here, ρ , \mathbf{v} , \mathbf{B} , and e are the density, velocity, magnetic induction, and the total energy, respectively, p the gas pressure, g_{\odot} the gravitational acceleration at the solar surface, and q the radiative source term

$$4\pi \rho \kappa (J - B), \quad (8)$$

where κ is the specific Rosseland mean opacity and B the local Planck function. J is the the mean intensity

$$J(\mathbf{r}) = \frac{1}{4\pi} \oint I(\mathbf{r}, \mathbf{n}) d\Omega \quad (9)$$

and ϵ is the internal energy from which the gas pressure is computed using Saha's equation taking Hydrogen ionization into account. Equation (6) is automatically satisfied if the initial field does so and if the numerical evaluation does not introduce magnetic monopoles due to numerical truncation errors. The actual form of the equations being solved, their finite volume representation, and the employed numerical technique are given in Steiner *et al.* (1994). Similar simulations of the flux intensification process in two spatial dimensions have been carried out by Hanami & Tajima (1991) and by Atroshchenko & Sheminova (1996), a three-dimensional calculation was done by Nordlund (1989).

The equations need to be supplemented by boundary conditions such as are summarized in Fig. 3. The “wave absorbing layer” damps outgoing waves in order to keep reflection at the closed top to a minimum and to suppress inwards propagating waves. The gas pressure is kept constant along the bottom boundary. Its value is adjusted in time so that the total mass within the computational domain remains constant.

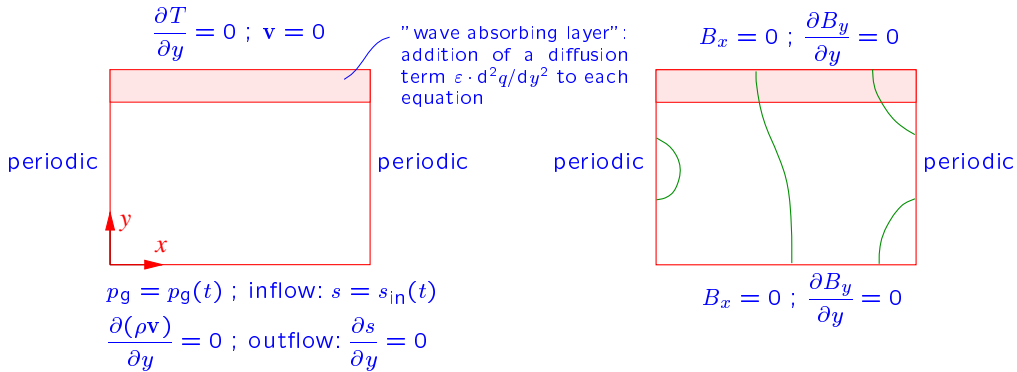


Figure 3. Boundary conditions on the MHD-equations for the simulation of magnetic flux-sheet formation. The left panel shows the conditions for the hydrodynamic variables, the right panel those for the magnetic field.

Grossmann-Doerth et al. (1998) start the simulation with a plane-parallel stratification according to a standard model of the solar atmosphere. The convectively unstable stratification is perturbed by a small velocity field, which subsequently grows until the system relaxes to instationary convective motion. Then a homogeneous vertical magnetic field is imposed onto the entire computational domain and the ensuing interaction between the magnetic field and the convective flow can be followed.

Fig. 4 shows a simulation with an imposed vertical homogeneous field of a strength of 100 G, other examples are discussed in Grossmann-Doerth *et al.* (1998). The field becomes rapidly concentrated at the location of the pre-existing downflow and a flux sheet with a field strength of about 2000 G at $\tau_{500} = 1$ forms within a time of about 3 min. Due to the relatively small magnetic flux density of the initial field the resulting flux-sheet width remains small (about 100 km at $\tau_{500} = 1$) and the backreaction of the field onto the convective motion is relatively feeble, at least in the initial phase. The downflow, which is further strengthened by radiative cooling of the plasma caught within the growing magnetic field, persists down to the open bottom of the computational domain and thus the flux sheet extends through the bottom boundary. For lack of material replenishing the downflow from the sides, the flux sheet becomes partially evacuated as can be seen from the depression of the $\tau_{500} = 1$ surface at the location of strong field concentration. This result changes drastically when the initial field is stronger (Grossmann-Doerth *et al.*, 1998). For example, if the same convective pattern as the one used in the simulation giving rise to Fig. 4 is superimposed with a 400 G field, a rebound of the downflow ensues followed by an upward traveling strong shock front. Fig. 5 shows for this case magnetic field lines and the velocity field after the rebound shock has traveled up to a height of about $z = 300$ km. At this position, the fractional pressure across the shock is about 30 and a thin layer of gas behind the front is 2600 K hotter than the ambient medium.

A rebound shock solution was recently also found by Takeuchi (1999) in one-dimensional calculations using the thin flux tube approximation. He con-

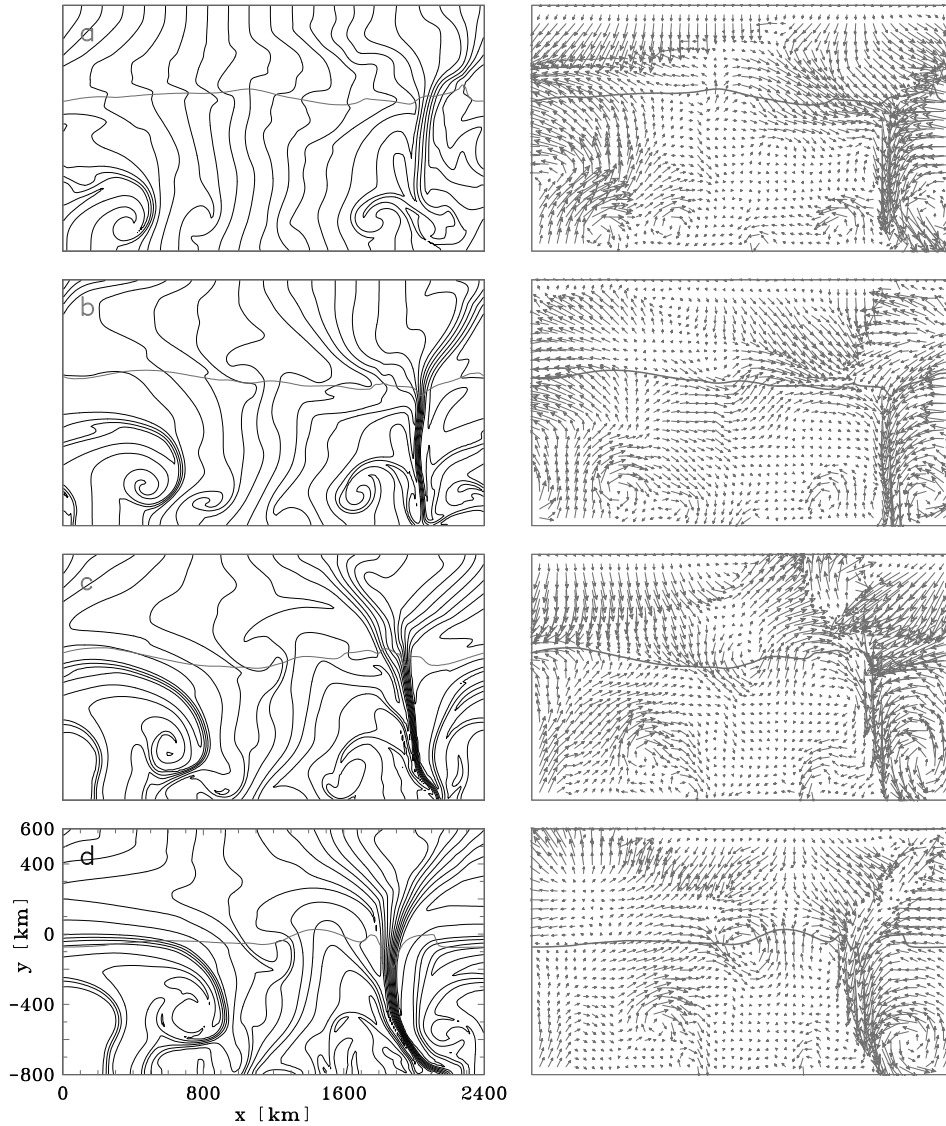


Figure 4. Formation of a magnetic flux sheet. Magnetic field lines (left) and velocity (right) at times 60, 115, 175, and 230 s after imposing an initially homogeneous magnetic field of 100 G on a previously established convection flow.

cludes that a shock solution ensues if the downflow in a collapsing flux tube is growing strong enough, which is the case if the initial plasma β of the tube undergoing convective collapse is small enough ($\beta_{\text{ini}} \geq 32$). In multidimensional calculations the initial plasma β , the perturbation velocities, and the mass content of the initial flux tube will be much determined by the local granular flow so that we expect Takeuchi's criterion for the occurrence of a rebound to become considerably modified in this case.

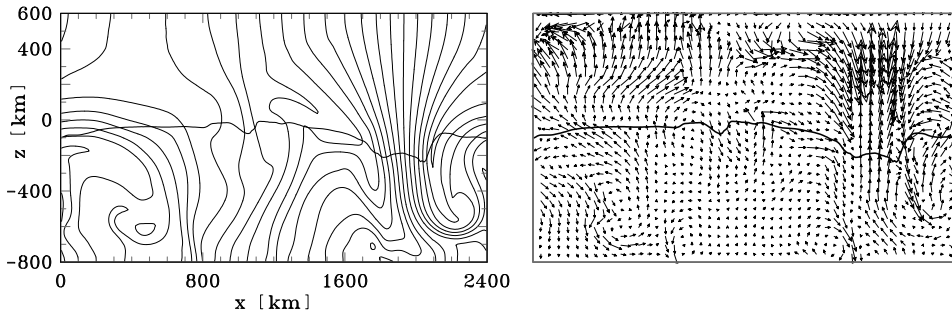


Figure 5. Formation of a magnetic flux sheet for the same initial flow field as used in Fig. 4 but with an initial field strength of 400 G. A rebound of the downflowing plasma entails a shock front, visible at $z \approx 300$ km, 250 s after imposition of the initial homogeneous field, which subsequently leads to a dispersal of the magnetic flux concentration.

3. Interaction of photospheric intense magnetic flux tubes with granular convection

The time period between the formation of a magnetic flux tube and its dissolution or reformation is characterized by a more quiescent phase during which the magnetic field strength remains more or less constant while flow velocities within the tube are small. Simulations of this quiescent phase, a snapshot of which is given in the top panel of Fig. 9, bring about the following three main results (Steiner et al., 1998).

First, there is a strong interaction between the convective plasma flow and the flux tube which leads to a swaying motion, bending, and horizontal displacement of the tube even though the plasma β is smaller than unity. One consequence of the swaying of the flux tube is the occasional exposition of an extended area of “hot wall” at a favorable angle toward an observer leading to a strong enhancement (and variation) of the continuum intensity of a magnetic flux concentration. Another consequence is the excitation of transversal tube waves, which couple with longitudinal compressional waves (Ulmschneider et al., 1991).

Second, the “squeezing” of the flux tube by convective plasma motion excites longitudinal flows within the tube that quickly shock in the photospheric layers of the tube atmosphere. These shock fronts (not to be confused with the shocks associated with the flux tube formation, mentioned in Sect. 2) leave distinct imprints in Stokes spectral lines of magnetic elements.

Third, during most of the simulation time the flux tube is bordered by strong, narrow downflows that are only occasionally perturbed by major variations in the convective flow field. They are maintained by the cooling of the gas surrounding the flux tube through the radiative energy flux into the magnetic region (Deinzer et al. 1984). The downflows evolve into ‘jets’: they become narrower with depth and accelerate strongly. They are fed by a corresponding horizontal flow that extends over a larger region and that may give rise to the bathtub effect in three-dimensional space, stabilizing the tube against inter-

changing. This flow, although pertaining to the field free plasma only, leads to a distinct asymmetry of Stokes spectral lines as will be discussed in Sect. 5.

4. The Spectral Signature of Flux-Sheet Formation

Carrying out the MHD-simulation we obtain for each time step all the necessary physical quantities (ρ , \mathbf{v} , T , p , \mathbf{B}) for the computation of synthetic spectral lines which then allows for a direct comparison with observed quantities. Since we seek information about the physical nature of magnetic elements we concentrate on spectral lines in the polarized light – the Stokes profiles. The synthetic Stokes profiles are computed by integration of the radiation transfer equation for polarized light along many vertical lines of sight distributed over the entire computational domain, followed by an averaging over the domain width. Examples of line-of-sight Stokes V profiles are shown in Fig.9. The averaging procedure mimics a spatially unresolved observation, but since the vertical magnetic field is strongly concentrated over only the small width of the flux sheet of about 100 km, the resulting Stokes V , Q , or U are essentially an average over just this small region. Note that a similar statement would *not* apply to Stokes I .

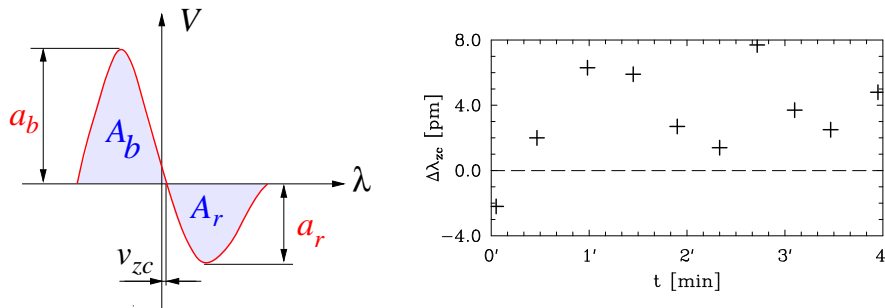


Figure 6. Left: Asymmetric Stokes V profile with Doppler zero-crossing-shift v_{zc} . Right: Temporal sequence of the zero-crossing-shift corresponding to the simulation of Fig. 4.

Fig. 6 (left) shows a typical Stokes V profile. v_{zc} is the so called (Doppler) zero-crossing-shift the amount by which the zero-crossing wave-length of the Stokes V profile is shifted with respect to the rest wavelength. The asymmetries between the amplitudes a_b and a_r and the areas A_b and A_r will be discussed in Sect. 5. Fig. 6 (right) shows the zero-crossing-shift (in pm) as a function of time of synthetic Stokes V profiles of Fe I 525.02 nm, corresponding to the simulation shown in Fig. 4 and averaged over the horizontal distance from $x = 1750$ – 2150 km. Due to the descending gas within and in the vicinity of the magnetic flux concentration during the formation process, all Stokes V profiles of the sequence shown in Fig. 4 and the corresponding zero-crossing-shift of Fig. 6 (right) are redshifted (with the exception of the first one at time $t = 0$). How does this redshift of the zero-crossing wavelength of synthetic Stokes V profiles compare to observations of magnetic elements?

4.1. Observation of flows in magnetic flux tubes

Measurements of the zero-crossing shift of Stokes V profiles in plage and network regions, carried out in the seventies and the early eighties, resulted in downflow velocities of up to 2.2 km s^{-1} . However, caution is indicated when interpreting these results as was pointed out by Solanki & Stenflo (1986) who noted that a spurious zero-crossing shift is measured as a consequence of insufficient *spectral* resolution. Spectral smearing of an asymmetric Stokes V profile with the blue lobe being larger than the red one (which is usually the case for plage and network magnetic elements at disk center) results in a redshifted zero-crossing wavelength.

Subsequently, high spectral resolution measurements, mainly carried out with the Fourier transform spectrometer at the Kitt Peak solar facility resulted in no significant zero-crossing velocities. For a comprehensive review see Solanki (1993).

“Epur si muove” – And yet it does move! – according to the following two recent measurements. Grossmann-Doerth *et al.* (1996) found a mean downflow velocity in network and plage magnetic elements of 0.8 km s^{-1} using the Zürich CCD-demodulator polarimeter (Povel, 1990). Measurements with HAO’s Advanced Stokes Polarimeter (ASP) (Elmore *et al.*, 1992) by Sigwarth *et al.* (1999) yield a mean downflow velocity of 0.73 km s^{-1} in magnetic elements of the quiet Sun, and 0.48 km s^{-1} in active region plages. These mean velocities are an average over 24,000 magnetic elements with Stokes V signals $> 0.20\%$ of the continuum intensity in the case of Grossmann-Doerth *et al.*, and 35,000 network elements and 93,000 active region elements, respectively, with Stokes V amplitudes $> 0.15\%$ in the case of Sigwarth *et al.* If the averaging would be restricted to the weakest network elements, say with amplitudes below 1%, the zero-crossing redshift would be rather in the order of 1 km s^{-1} . Evidence for a mean downflow in magnetic elements was also found by Martínez Pillet *et al.* (1997). Note that single weak magnetic elements show a scatter of up to $\pm 5 \text{ km s}^{-1}$ around the mean value.

The difference with respect to older measurements resulting in no significant zero-crossing shift is due to the high sensitivity of the employed polarimeters and to the better spatial resolution compared to the FTS data, which permits the sampling of magnetic elements with small magnetic flux. These elements became swamped by the elements of largest flux within a resolution patch in earlier measurements. Magnetic elements with a Stokes V signal ($\geq 2\%$) show negligible zero-crossing shifts also in these latest measurements.

Because the weakest Stokes V profiles that enter the statistics of Grossmann-Doerth *et al.* (1996) and Sigwarth *et al.* (1999) are strongly affected by noise, one might argue that noise could introduce once again a spurious zero-crossing redshift similar to the effect of insufficient spectral resolution. However, Sigwarth *et al.* show that noisy profiles with *negative* area asymmetry show a redshifted zero-crossing as well, contrary to what one would expect if this argument were true. This strongly suggests that the mean downflow in magnetic elements apparent in the most recent measurements is real.

4.2. Convective collapse contribution to the zero-crossing redshift

The scatter plots of the zero-crossing shift versus Stokes V amplitude shown in the works of Grossmann-Doerth *et al.* (1996) and Sigwarth *et al.* (1999) represent magnetic elements in various stages of their evolution. Many of them may be in a quiescent phase of their life, giving rise to “normal” Stokes profiles with a small zero-crossing shift. Others correspond to magnetic elements in the stage of dissolution, coalescence with other elements, cancellation with opposite polarity field, or in the stage of formation through convective collapse. We expect flux tubes in the formation stage to produce a zero-crossing redshift because of the downdraft within the tube. They contribute to a net ensemble-averaged positive zero-crossing redshift. If the downdraft is strong enough a rebound shock as shown in Fig. 5 ensues, leading to an upflow. These occasional events produce blueshifted zero-crossings but do not cancel the prevailing red-shift.

5. Stokes V Area and Amplitude Asymmetries

Stokes V profile asymmetries provide a useful diagnostic for the gas motion within magnetic elements and in their close surroundings. Solanki & Pahlke (1988) have given a easy-to-remember formula relating the sign of the area asymmetry to the gradients of the absolute magnetic field strength and the velocity along a line of sight:

$$\frac{d|B|}{d\tau} \cdot \frac{dv(\tau)}{d\tau} = \begin{cases} < 0 & \Rightarrow \delta A > 0 \\ > 0 & \Rightarrow \delta A < 0 \end{cases}, \quad (10)$$

where $\delta A = (A_b - A_r)/(A_b + A_r)$, with A_b and A_r being the area of the red and blue lobe of the Stokes V profile, respectively (see Fig. 6 [left]). A rigorous derivation of Eq. 10 can be found in Sanchez Almeida and *et al.* (1989) and an extension to transverse fields in Sanchez Almeida (1998).

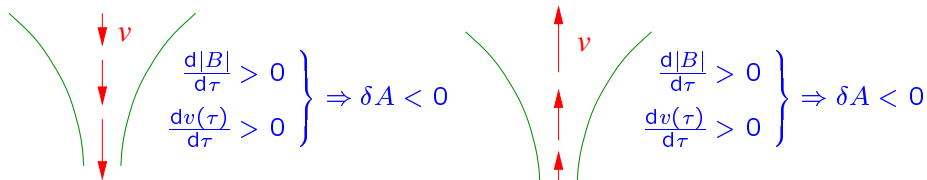


Figure 7. Sign of the Stokes V area asymmetry formed along the flux-tube axis with an accelerating downflow (left) or upflow (right).

Fig. 7 shows the result when applying Eq. 10 to a line of sight along the flux-tube axis, when an accelerating downflow or upflow is present. An accelerating downflow occurs during the convective collapse while an accelerating upflow ensues from the “inverse collapse” phase which may take place after the rebound

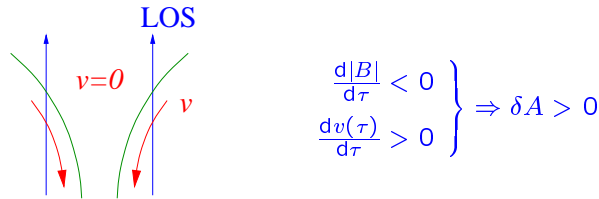


Figure 8. Sign of the Stokes V area asymmetry formed along lines of sight that pass through the expanding flux-tube boundary.

of a downflow. These two situations yield a negative area asymmetry, which is at variance with the observed positive mean value¹ of δA .

The situation changes completely for lines of sight that pass through the expanding boundary of the flux tube (the onset of the magnetic canopy as sketched in Fig. 8), which contribute with a positive δA (Grossmann-Doerth *et al.*, 1988,1989; Bünte *et al.*, 1993a). This is due to the downflow in the close vicinity of the flux tube, which is driven by the radiative heat loss of the surrounding gas into the flux tube (see Sect. 3). Thus, at the location where the line of sight crosses the flux-tube boundary, a strong negative field strength gradient collocates with a strong positive velocity gradient, producing a positive area asymmetry. This positive contribution seems most of the time to outweigh the negative contribution of the tube core.

How realistic are the sketches shown in Figs. 7 and 8? We have no means to answer this question observationally, because it addresses fine-structure of magnetic elements that is far beyond the spatial resolution capabilities of present time solar telescopes, but we may attempt an answer by examination of snapshots from a simulation. Fig. 9 shows an example of a snapshot from a simulation on the interaction of granular flow with a magnetic flux sheet (Steiner *et al.*, 1998 [panel b of Fig. 1]). Results of this simulation are summarized in Sect. 3. The temperature, the velocity field, and representative magnetic lines of force are shown. The horizontally running curve indicates the surface of optical depth unity, $\tau_{500} = 1$. In contrast to Fig. 4, this simulation was started with a mature strong magnetic flux concentration and the bottom boundary was closed to the fluid so that the flux sheet remained intact over the full simulation period of 40 min.

When computing the Stokes V profiles that emanate from vertical lines of sight distributed over the horizontal interval between 600 and 1380 km of Fig. 9, we find that positive area asymmetries result in the two regions labeled with “+”, while the lines of sight in the middle region labeled with “-” contribute negative area asymmetries, exactly as expected from the simple sketches of Figs. 7 and 8, based upon Eq. 10. The actual profiles emanating from each line of sight is shown in Fig. 9, where the mean amplitude, the amplitude asymmetry, the area asymmetry (all in %), and the zero-crossing shift in mÅ are printed (from top to bottom) at the right side of each panel. In addition, positive and negative

¹There is a considerable scatter of the measured area asymmetry of up to 100% for weak polarization signals. However, the quiet Sun average value is $\bar{\delta A} = 6\%$ according to Sigwarth *et al.* (1999).

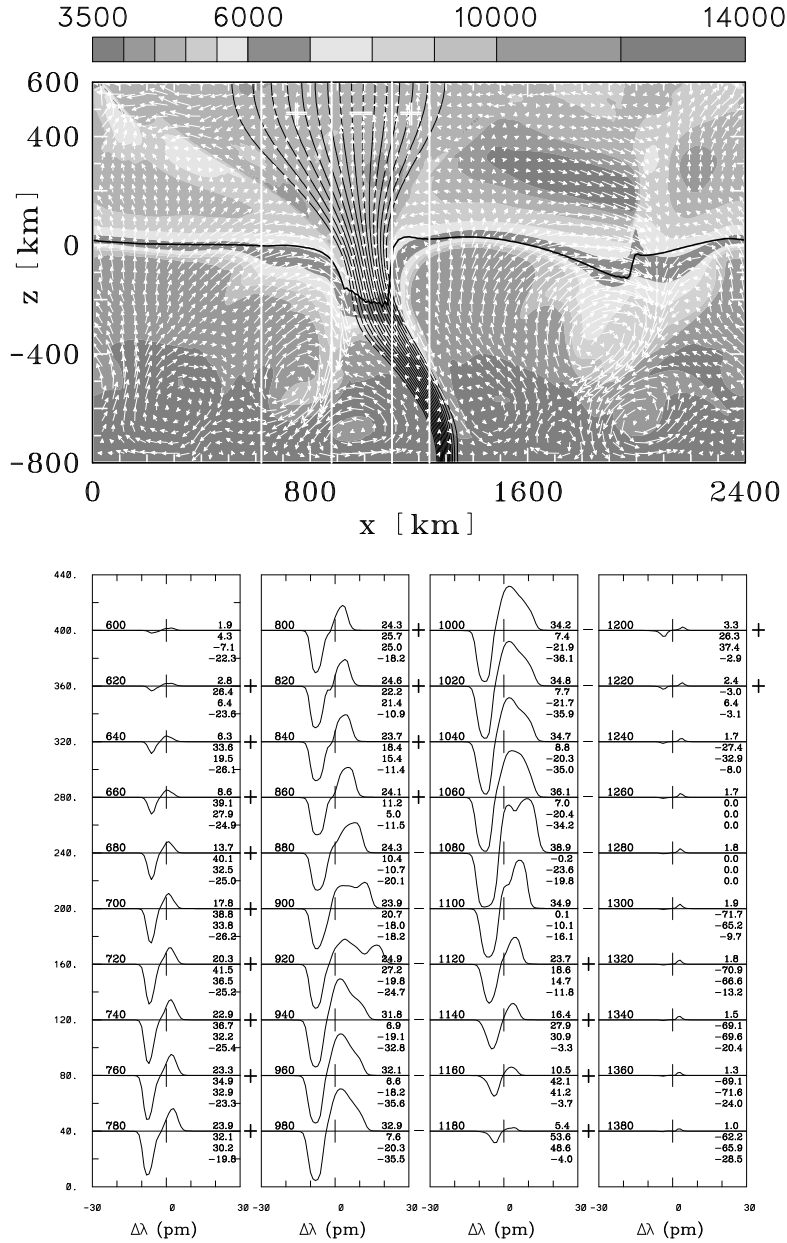


Figure 9. Simulation snapshot (see text for explanations). Stokes V profiles corresponding to vertical lines of sight distributed over a horizontal span from 600 – 1380 km.

area asymmetries are annotated in the right margin with a plus and a minus sign, respectively.

Half of the snapshots to which series Fig. 9 belongs show a similar behaviour with respect to δA , while in the other half the flow within the flux sheet does not correspond to either case of Fig. 7 and therefore produces a positive δA too.

We conclude that the measured, spatially unresolved Stokes V area asymmetry of network elements results from a delicate balance of negative and positive contributions due to the internal structure of the elements. The simulations also suggest that the amplitude asymmetry, $\delta a = (a_b - a_r)/(a_b + a_r)$, is not subject to a similar balance and therefore shows larger and almost always positive values. Bellot Rubio *et al.* (1997) were led to a similar conclusion by the inversion of observed Stokes V profiles based upon a multi-component model. However, the uniqueness of this inversion was put into question by Frutiger & Solanki (1998).

A statistical analysis similar to the ones made by Grossmann-Doerth *et al.* (1996) and Sigwarth *et al.* (1999) has been carried out with synthetic profiles of the above-mentioned simulation series (discussed in Sect. 3), considering the individual snapshots to be independent single magnetic elements (Grossmann-Doerth, 1997). This then allows the determination of mean values of δA , δa , and v_{zc} . Notice, however, that this simulation run represents a single flux sheet of a given size in a certain, rather stable and quiescent phase, while the observational data encompass magnetic elements of a larger variety and in different phases of their life. Nevertheless in Table 1 we attempt a comparison of mean synthetic Stokes profile parameters with observed ones.

Table 1. Mean values of Stokes V profile parameters. The first two rows are derived from synthetic profiles of simulation models, the rest from observations.

Ref.	Instrument	Region	FeI	δa	δA	v_{zc}
1	<i>Simulation</i>	<i>temporal distrib.</i>	<i>6302.5</i>	<i>14.9</i>	<i>0.4</i>	<i>0.74</i>
1	Simulation	temporal distrib.	5250.2	14.1	-2.6	0.67
2	<i>ASP</i>	<i>Quiet Sun average</i>	<i>6302.5</i>	<i>15.0</i>	<i>6.0</i>	<i>0.73</i>
2	ASP	Active region	6302.5	9.4	0.7	0.48
3	Zimpol	Quiet Sun average	5250.2	14.8	3.9	1.0
4	ASP	Plage average	6302.5	10.0	3.0	0.2
5	FTS	Network	5250.2	22.4	7.4	<0.3
5	FTS	Plage	5250.2	16.2	6.6	<0.3

¹Steiner *et al.*: 1998, ApJ 495, 468; ²Sigwarth *et al.*: 1999, A&A, in preparation;
³Grossmann-Doerth *et al.*: 1996, A&A 315, 610; ⁴Martínez Pillet *et al.*: 1997, ApJ 474, 810; ⁵Solanki S.K.: 1993, Space Science Review 63, 1

Mean values for δA , δa , and v_{zc} of the synthetic FeI 6302.5 spectral line of 14.9%, 0.4%, and 0.74 km s⁻¹, respectively are obtained. This is in good agreement with the observational results of Sigwarth *et al.* (1999) for magnetic elements of quiet Sun regions for the same line (15%, 6%, and 0.73) with the exception of the area asymmetry, which is rendered too small by the simulation.

One reason for this might be that the boundary of real flux tubes is very “sharp”, *i.e.*, the transition from internal to external atmosphere is confined within about 10 km. This leads to strong gradients in magnetic field strength and velocity and therefore to an enhanced area asymmetry compared to the case of the simulation where the flux sheet boundary is more diffuse. Another reason one could think of is that for geometric reasons more lines of sight pass through the canopy region in the case of a flux tube compared to a sheet. However this effect is canceled by a reduced expansion rate of the tube versus the sheet for the same geometric reason.

Yet another reason for the low value of δA may be the peculiar extension of the far red wing characteristic of synthetic Stokes V profiles. This extension of the red wing is, to a lesser degree, also present in observed Stokes V profiles. It increases the area of the red lobe and thus reduces δA . The origin of the extended red wing was traced back to a downflow layer within the flux tube located close to the tube surface. It is induced by the persistent downflow in the surroundings of the flux tube via drag forces mediated by turbulent viscosity. Because of the limited spatial resolution of 10 km, this effect is overestimated in the simulations and therefore artificially reduces δA of synthetic Stokes V profiles.

6. Conclusions

1. The fragmentation of G-band bright points is probably due to the interchange instability of small-scale magnetic flux tubes.
2. Magnetic flux-tubes in the stage of formation produce red-shifted Stokes profiles. Consequently, they must be an important contributor to the observed mean redshift of the Stokes V zero-crossing of magnetic elements in network and plage regions.
3. The net Stokes V area asymmetry of a single magnetic element is the result of a delicate balance between a positive contribution by lines of sight that pass through the expanding tube surface (canopy) and a negative contribution by lines of sight through the core of the flux tube.
4. The simulation of the quiescent stage of flux tubes reproduce the observational results except of a discrepancy in the area asymmetry of Stokes V that is possibly due to the boundary layer of flux-sheets being smaller than the resolution limit of the simulation of 10–20 km and/or to the coacceleration of magnetized material in a turbulent boundary layer between the flux tube and the strong external downflow that gives rise to an extended red wing of Stokes V profiles.

Acknowledgments. I would like to thank M. Schüssler for critically reading the manuscript and U. Grossmann-Doerth for providing Fig. 9 (bottom) and the data for Fig. 6 (right).

References

- Atroshchenko I.N. & Sheminova V.A., 1996, Кинемат. и Физ. Небесн. Тел, 12, 32
- Bellot Rubio L.R., Ruiz Cobo B., & Collados M., 1997, A&A, 478, L45
- Berger T.E., 1996, Thesis, Stanford University
- Berger T.E. & Title A.M., 1996, ApJ, 463, 365
- Berger T.E., Löfdahl, M.G., Shine, R.S., & Title A.M., 1998, ApJ, 495, 973
- Berger T.E., Schrijver C.J., Shine R.A., Tarbell T.D. Title A.M., & Scharmer G., 1995, ApJ, 454, 531
- Bünte M., 1993, A&A, 276, 236
- Bünte M., Solanki S.K. & Steiner O., 1993a, A&A, 268, 736
- Bünte M., Steiner O., & Pizzo V.J., 1993b, A&A, 268, 299
- Deinzer, W., Hensler, G., Schüssler, & M., Weisshaar, E.: 1984, A&A, 139, 435
- Elmore, D.F., Lites, B.W., Tomczyk, S., Skumanich, A.P., *et al.*, 1992, SPIE (Society of Photo-Optical Instrumentation Engineers), 1746, 22
- Frutiger C. & Solanki S.K., 1998, A&A, 336, L65
- Galloway D.J., Proctor M.R.E., & Weiss N.O., 1977, Nature, 266, 686
- Grossmann-Doerth: 1997, *The Betaslab Brief*, Kiepenheuer-Institut, internal report
- Grossmann-Doerth U., Keller C.U., & Schüssler M., 1996, A&A, 315, 610
- Grossmann-Doerth U., Schüssler M., & Solanki S.K., 1988, A&A, 206, L37
- Grossmann-Doerth U., Schüssler M., & Solanki S.K., 1989, A&A, 221, 338
- Grossmann-Doerth U., Schüssler M., & Steiner O., 1998, A&A, 337, 928
- Hanami H. & Tajima T., 1991, ApJ, 377, 694
- Hasan, S.S., 1983, in proc. IAU Symp. 102, p. 73
- Hasan, S.S., 1984, ApJ, 285, 851
- Hasan, S.S., 1985, A&A, 143, 39
- Hasan, S.S., 1986, MNRAS, 219, 357
- Martínez Pillet V., Lites B.W., & Skumanich A., 1997, ApJ, 474, 810
- Massaglia S., Bodo G., & Rossi, P., 1989, A&A, 209, 399
- Meyer F., Schmidt H.U., & Weiss N.O., 1977, MNRAS, 179, 741
- Muller R.A., 1985, Sol. Phys., 100, 237
- Nordlund Å, 1989, in Solar and Stellar Granulation, R.J. Rutten & G. Severino (eds.), NATO ASI Ser. C-263, Kluwer, Dordrecht, 453
- Parker E.N., 1963, ApJ, 138, 552
- Parker E.N., 1975, Solar Phys., 40, 291
- Parker E.N., 1978, ApJ, 221, 368
- Piddington J.H., 1975, Astrophys. Space Sci., 34, 347
- Povel, H., Aebbersold, H., & Stenflo, J.O., 1990, Applied Optics, 29, 1186
- Roberts B. & Webb A.R., 1978, Sol. Phys., 56, 5
- Sanchez Almeida J., 1998, ApJ, 497, 967
- Sanchez Almeida J., Collados, M., & Del Torro Inesta J.C., 1989, A&A, 222, 311
- Schüssler M., 1984, A&A, 140, 453
- Schüssler M., 1990, in proc. IAU Symp. 138, p. 161
- Sigwarth, M., Balasubramaniam, K.S., & Knölker, M., 1999, A&A, in prep.
- Simon G.W. & Weiss N.O., 1997, ApJ, 489, 960
- Solanki S.K., 1993, Space Sci. Rev., 63, 1

- Solanki S.K. & Pahlke K.D., 1988, A&A, 201, 143
Solanki S.K. & Stenflo J.O., 1986, A&A, 170, 120
Spruit H.C., 1979, Sol. Phys., 61, 363
Spruit H.C. & Zweibel E.G., 1979, Sol. Phys., 56, 5
Steiner O., Grossmann-Doerth, U., Knölker M., & Schüssler M., 1998, ApJ, 495, 468
Steiner O., Knölker M., & Schüssler M., 1994, in Solar Magnetism, R.J. Rutten & C.J. Schrijver (eds.), NATO ASI Ser. C-433, Kluwer, Dordrecht, 181
Takeuchi A., 1993, Publ. Astron. Soc. Japan, 45, 811
Takeuchi A., 1995, Publ. Astron. Soc. Japan, 47, 331
Takeuchi A., 1999, ApJ, submitted
Ulmschneider P., Zähringer K., & Musielak Z.E., 1991 A&A, 241, 625
Unno W. & Ando H., 1979, Geophys. Astrophys. Fluid Dynamics, 12, 107
Venkatakrishnan P., 1983, J. Astrophys. Astr., 4, 135
Venkatakrishnan P., 1985, J. Astrophys. Astr., 6, 21
Venkatakrishnan P., 1986, Nature, 322, 156
Webb A.R. & Roberts B., 1978, Sol. Phys., 59, 249
Webb A.R. & Roberts B., 1980, Sol. Phys., 68, 87
Weiss N.O., 1966, Proc. Roy. Soc. Lon., A 293, 310 V, Lecture Notes in Physics Vol. 291, Springer-Verlag, p. 54